High-resolution transmission electron microscopy investigation of diffusion in metallic glass multilayer films

S.V. Ketov [a, *, 1], Yu P. Ivanov [a, b, h, 1], D. Şopu [a, c], D.V. Louzguine-Luzgin [d, e],
C. Suryanarayana [f], A.O. Rodin [g], T. Schöberl [a], A.L. Greer [h], J. Eckert [a, i]

[a] *Erich Schmid Institute of Materials Science, Austrian Academy of Sciences, Jahnstraße 12, A-8700 Leoben, Austria*
[b] *School of Natural Sciences, Far Eastern Federal University, 690950 Vladivostok, Russia*
[c] *Institut für Materialwissenschaft, Technische Universität Darmstadt, Otto-Berndt-Str. 3, D-64287 Darmstadt, Germany*
[d] *WPI Advanced Institute for Materials Research, Tohoku University, 2-1-1 Katahira, Sendai 980-8577, Japan*
[e] *Mathematics for Advanced Materials-OIL, National Institute of Advanced Industrial Science and Technology (AIST), Sendai 980-8577, Japan*
[f] *Department of Mechanical and Aerospace Engineering, University of Central Florida, Orlando, FL 32816-2450, USA*
[g] *National University of Science and Technology "MISiS", Moscow 119049, Russia*
[h] *Department of Materials Science & Metallurgy, University of Cambridge, Cambridge CB3 0FS, UK*
[i] *Department Materials Physics, Montanuniversität Leoben, Jahnstraße 12, Leoben A-8700, Austria*

A B S T R A C T

Lack of plasticity is one of the main disadvantages of metallic glasses. One of the solutions to this problem can be composite materials. Diffusion bonding is promising for composite fabrication. In the present work the diffusion process in glassy multilayer films was investigated. A combination of advanced transmission electron microscopy (TEM) methods and precision sputtering techniques allows visualization and study of diffusion in amorphous metallic layers with high resolution. Multilayered films were obtained by radio frequency sputter deposition of Zr-Cu and Zr-Pd. The multilayers were annealed under a high vacuum (10^{-5} Pa) for 1 and 5 h at 400 °C, that is, well below the crystallization temperatures but very close to the glass-transition temperatures of both types of the glassy layer. The structural evolution in the deposited films was investigated by high-resolution transmission electron microscopy. It was observed that, despite the big differences in the atomic mass and size, Pd and Cu have similar diffusion coefficients. Surprisingly, 1 h of annealing results in formation of metastable copper nanocrystals in the Zr-Cu layers which, however, disappear after 5 h of annealing. This effect may be connected with nanovoid formation under a complex stress state evolving upon annealing, and is related to the exceptionally slow relaxation of the glassy layers sealed with a Ta overlayer.

1. Introduction

Metallic glasses are promising structural and functional materials [1]. Owing to their disordered atomic structure, they exhibit exceptionally high yield stress and large elastic limit [2]. However, lack of long-range order and pronounced localization of plastic deformation at low temperatures result in poor ductility [3]. Shear-band propagation is the main mechanism governing the plastic deformation of metallic glasses [4,5]. Generation of multiple shear bands upon deformation increases the plasticity of metallic glasses [6]. One of the ways to achieve this is the formation of a composite material [7,8]. Dendrites of a soft crystalline phase in a glassy matrix obstruct the propagation of the shear bands and also cause them to branch. However, it is hard to control the formation of the crystalline phase upon casting, and there is only a limited variety of suitable alloy compositions that form composites with the required structure upon quenching. Glass/glass composites experience the same problem of structure control as crystalline/glass ones [9]. Another solution for composite preparation can be sintering of a powder mixture [10]. However, powders usually have a surface native oxide which degrades the sintering ability. Oxide layers also introduce weak zones into the resulting bulk sample, giving poor resistance to crack propagation upon plastic deformation. Bonding of glassy

* Corresponding author.
E-mail address: Sergey.Ketov@oeaw.ac.at (S.V. Ketov).
[1] Authors made an equal contribution to the paper.

alloys can be also achieved by Joule heating [11] as well as by laser [12,13], electron-beam [14,15] and friction [16] welding.

Long-term low-temperature diffusion bonding might be helpful in composite fabrication. Diffusion in metallic glasses became a topic of wide interest after the discovery of interface reactions between certain crystalline metallic film layers which lead to formation of an amorphous phase [17,18]. Interdiffusion in glassy multilayers revealed a dependence of the diffusion coefficient on the layer thickness and the composition of the glass [19,20]. Various aspects of diffusion in metallic glasses have been summarized by Faupel et al. [21].

However, since those studies, structure-imaging techniques and knowledge about the structure of metallic glasses have made huge steps forward. Moreover, in recent years the concept of diffusion bonding attracted new interest. It was shown that this method works quite well for bonding metallic glasses to each other [22] and to pure metals [23,24]. Recently, there have also been attempts to simulate diffusion in metallic glasses [25,26]. It was also shown that magnetron sputter deposition can lead to the formation of metallic-glass multilayers with the interlayer interface having a mixture of immiscible atoms such as Fe and Cu and this interface widens upon annealing at elevated temperatures [27].

In 1947, Smigelskas and Kirkendall [28] reported on zinc diffusion in brass. It was found that, due to the different diffusion rates of copper and zinc, the interdiffusion interface moves from its original position. This was and is an excellent example of vacancy-mediated diffusion. One of the side effects of the asymmetric diffusion is the formation of pores during the diffusion process [29]. The size and amount of the pores can be controlled by controlling the temperature and duration of annealing. Having no long-range order and, therefore, no vacancies, it is unclear if the Kirkendall effect can be used to create controlled porosity in metallic glasses which could be favorable for improving the mechanical properties [30]. The size and amount of pores can play an important role for the plasticity of metallic glasses. A high amount of pores results in deterioration of the yield strength of the material. Voiding was found during interdiffusion in Zr-Ni amorphous multilayers [31]; however, there have been no further reports of this effect in metallic glasses.

In the present work, two alloy systems, namely Zr-Cu and Zr-Pd, were chosen as typical examples of 'hard' and 'soft' bonded metallic glasses [32,33]. 'Hard' and 'soft' bonding reflects the structure of the atomic bonds in the system. 'Hard' bonding in comparison to the 'soft' shows small or no difference of the sum of atomic radii for atomic pairs from the sum of Goldschmidt radii in corresponding crystalline compounds and can be viewed as a system of hard spheres. Chosen glass-forming systems are binary, which simplifies the studies of the diffusion. Atomic radius and mass are significantly different for Cu and Pd; therefore, mobility and diffusivity of these atoms are expected to be different as well. Here, we present a thorough investigation of atomic diffusion in multilayer metallic glassy films, where the layers contain elements with large differences in atomic size, mass, and diffusivity and show that modern high-resolution transmission electron microscopy (HRTEM) can be used as a universal and powerful tool to conduct such investigations.

2. Results and discussion

Fig. 1a shows a cross-sectional view of an as-deposited Zr-Pd/Zr-Cu multilayered film obtained by transmission electron microscopy (TEM). The periodic structure of the film with a bilayer thickness of 60 nm is clearly visible in the bright-field (BF) image mainly because of the difference in atomic numbers of Cu ($Z = 29$, lighter layers) and of Pd ($Z = 46$, darker layers). One can also observe

protective Ta cap layers on both sides of the multilayer film (Fig. 1a, black stripes).

The structure of the as-deposited multilayer is amorphous. However, there is a small amount of slightly dark spots in the Cu-Zr layers. HRTEM images reveal that some of these spots contain nanocrystals (NCs). One can clearly see crystalline lattice fringes on the HRTEM image and corresponding spots on the fast-Fourier-transform (FFT) pattern (Fig. 1c, region 1). In contrast, no NCs were found in the Zr-Pd layers (Fig. 1c, region 3). The crystallite size is very small ($1-2$ nm) and the diffraction pattern corresponds to pure fcc Cu. The sputtering conditions possibly allowed fast atomic surface diffusion of the lighter copper upon deposition and formation of NCs near the edges of the Zr-Cu layers. The number of these NCs in the as-deposited multilayered film is very small (only one was found in Fig. 1a), and they were found only in Zr-Cu layer (Fig. 1a).

The annealing was conducted after deposition in the sputtering chamber under high vacuum (10^{-5} Pa). The conditions were as follows: $T = 400\,°C$, $t = 1$ h and 5 h. The temperature was chosen to be high enough to activate diffusion and at the same time to not crystallize the film. The crystallization behavior of these particular Zr-Cu and Zr-Pd films was not studied in the present work, and it is unknown how it can be influenced by the layered film structure and the limited thickness of the layers. It is known that ribbons of $Zr_{65}Pd_{35}$ crystallize in two stages: a quasicrystalline phase precipitates first and subsequently transforms to Zr_2Pd and Zr phases. The crystallization temperature (T_x) of the Zr-Pd amorphous alloy in the present work ($Zr_{62}Pd_{38}$, at.%) should not differ significantly from that of $Zr_{65}Pd_{35}$ which is 500 °C for melt-spun ribbons [34]. The crystallization behavior of ribbons and films was found to be very similar. Glassy ribbons of $Zr_{54}Cu_{46}$ crystallize at about $T_x = 440\,°C$ [35,36]. DC-sputtered films of the same composition have a crystallization temperature $T_x = 445\,°C$. Therefore, the chosen annealing temperature of 400 °C is less than the crystallization temperatures of the films of both compositions. It also very close to the glass-transition temperature T_g of both alloys ($T_g = 403\,°C$ for $Zr_{54}Cu_{46}$ [36] and $T_g \approx 420\,°C$ for $Zr_{62}Pd_{38}$ [34,37]).

Annealing the layered film for 1 h leads to nucleation of Cu NCs (Fig. 2). Diffraction patterns do not show any intermetallic compound formation. Interestingly, nucleation of these NCs takes place close to the center of the Zr-Cu layers (Fig. S4b). The NCs form large agglomerates of more than 5 nm in size. The size of the individual NCs is $1-1.5$ nm. As in the as-deposited state, no crystallization was found in the Zr-Pd layers.

After 1 h of annealing one can find bright spots in the high-angle annular dark-field (HAADF) images of the Zr-Cu layers. An enhanced atomic order is observed in these zones which corresponds to the scattering from copper NCs (Fig. 3b). Cu NCs are thermodynamically unstable in the Zr-Cu system with around 1:1 concentration ratio and dissolve upon further annealing. No contrast variation from copper NCs can be found in the TEM image after 5 h of annealing (Fig. 3c). However, it is also possible that after 5 h of annealing the copper NCs are less visible because of the redistribution of the elements and a general increase of the film density due to structural relaxation of the amorphous film. Analysis of the distribution of spots showed that number of spots increases from layer close to the substrate toward the layer close to the surface (see Supplementary Materials Fig. S4b). This can be the sign that excess volume migrates to the surface of multilayer during annealing. In each individual Zr-Cu layer, most spots are near the center of the layer (Fig. S4c).

As observed by TEM, the Ta layers are polycrystalline and do not show structural changes during annealing. As the multilayer was deposited on a silica substrate the diffusion of Si into Ta is difficult. Our compositional study by energy-dispersive X-ray (EDX) did not
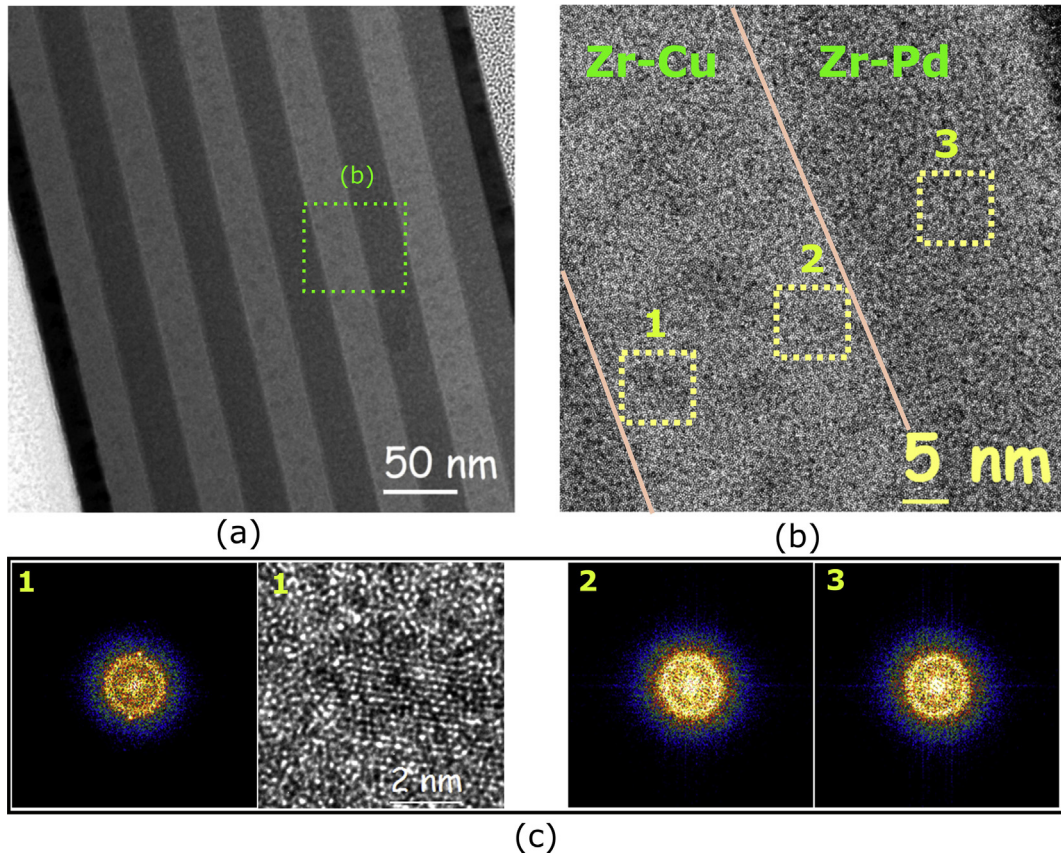
Fig. 1. a) BF TEM cross-sectional image of an as-deposited Zr-Pd/Zr-Cu multilayered film (substrate is on the left side of the image); (b) high-resolution TEM (HRTEM) image; and (c) fast-Fourier-transform (FFT) patterns from different regions (marked by numbers: 1 and 2 in a Zr-Cu layer, and 3 in a Zr-Pd layer). Lines are used for visual separation of the different film layers. The figure also contains a magnified HRTEM image of region 1 in the TEM image. The crystalline reflections in the FFT pattern from region 1 (2.04 ± 0.04 Å) correspond to fcc Cu(111) (2.06 Å). TEM, transmission electron microscopy; BF, bright-field.
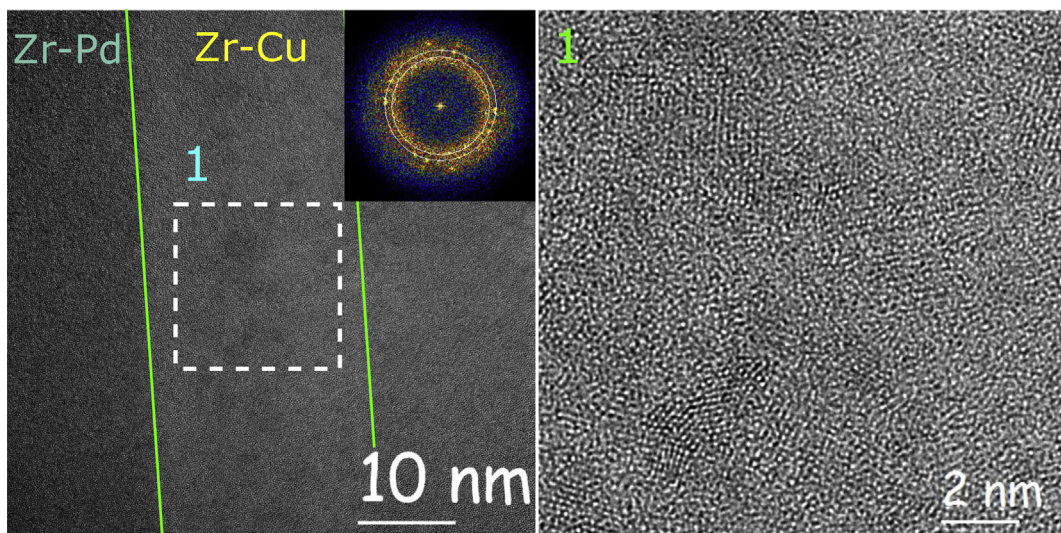

Fig. 2. BF TEM image of an as-deposited Zr-Pd/Zr-Cu multilayered film after 1 h of annealing together with an HRTEM image and an FFT pattern (inset) of the Zr-Cu layer (designated region 1). The diffraction rings correspond to the 2.06 ± 0.04 Å − fcc Cu(111) (2.06 Å) and 1.80 ± 0.04 Å − fcc Cu(002) (1.79 Å) planes. Green lines are used for visual separation of the different film layers. TEM, transmission electron microscopy; BF, bright-field; FFT, fast-Fourier-transform; HRTEM, high-resolution TEM.

indicate any Si diffusion into the amorphous multilayered structure.

The formation of the Cu NCs also was confirmed by EDX mapping analysis of the Zr-Cu layers (Fig. 4). The

nanocrystalline zones formed after 1 h of annealing that are observed in the HAADF images clearly correspond to the copper-enriched zones in the EDX maps (marked by arrows in Fig. 4).
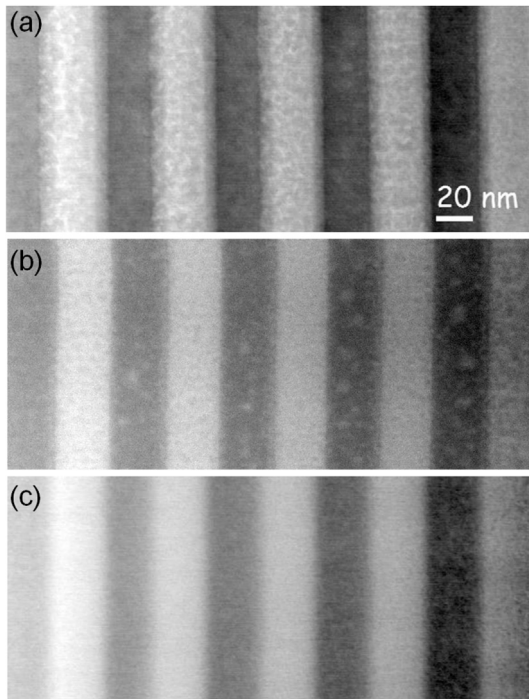
Fig. 3. High-angle annular dark-field (HAADF) images: as-deposited film (a), after 1-h annealing (b), after 5-h annealing (c). Darker regions correspond to Zr-Cu, brighter regions to Zr-Pd. Left part of the images is closer to the substrate.

The interdiffusion between Cu-Zr and Pd-Zr layers as well as its evolution upon low-temperature annealing was evaluated using EDX studies. It is clearly seen that the boundary between the layers becomes wider upon annealing (Fig. 5). Analysis of the distribution profiles of Pd and Cu shows that both species diffuse across the interface of the film layers, whereas the distribution of the Zr atoms does not change much.

Right after deposition, the Zr-Pd and Zr-Cu regions in the HAADF images contain a lot of contrast fluctuations (Fig. 3a). These fluctuations can be connected with density variation under the condition that the thickness of the electron-transparent foil does not vary significantly (see Suppl. Fig. S1). The contrast variations disappear after annealing because of the relaxation of excess volume, giving a more homogeneous distribution of the atoms. One can also see that the initially large variations of the composition profiles smoothen after the annealing (Fig. 5).

To investigate the changes in the atomic structure of the amorphous multilayers upon annealing, we used a reduced radial distribution function (RRDF) analysis of the HRTEM images. Square areas with an edge size of 3.0 nm, randomly distributed on the HRTEM images, were chosen to build the diffraction patterns of the Cu-Zr and Pd-Zr layers by FFT after different annealing times. The RRDF curves were calculated by running the Digital Micrograph script RDF TOOLS [38]. For each annealing time, we prepared the TEM sample separately, and therefore, the general peak intensity of the RDF curves cannot be compared directly. However, this fact does not influence the positions of the peaks and the relative peak-intensity distributions. The calculated atom-atom bond lengths are shown by the vertical lines in Fig. 6(a) and (b). These lengths in the first coordination shell were calculated as a sum of the Goldschmidt metallic radii of the corresponding atoms [39]. One can see that the RRDF of the Zr-Pd layer does not change much upon annealing (Fig. 6a). Interestingly, the first peak position moves closer toward Zr-Zr and Zr-Pd bond lengths. This can be interpreted as a chemical bond evolution where the system tries to rearrange its structure for crystallization of the Zr_2Pd phase which is stable at such composition and conditions. The splitting of the second peak indicates enhanced ordering in the glass due to relaxation.

The RRDF of the Zr-Cu layer after deposition (Fig. 6b) is very similar to those obtained from synchrotron X-ray and neutron studies of ribbons of the same composition [40]. Annealing for 1 h changes the structure of the Zr-Cu layers significantly (Fig. 6b). Here, we calculated two RRDFs from different regions of the layer: one was taken from a region with NC and the other from a fully amorphous region. For regions with copper crystals, the first peak splits and the Cu-Cu peak becomes more pronounced. Annealing for 5 h results in disappearance of the NCs and the Cu-Cu peak is less intense, whereas the Zr-Zr shoulder of the first peak intensifies.

As the multilayer films are deposited under the same conditions and only differ by the annealing time, one can use nanoindentation measurements to investigate the influence of annealing on film hardness. The apparent hardness and the indentation elastic modulus (E) of the multilayers increase with longer annealing time (Table 1). This behavior can be explained by both an increase of internal stresses as well as general structural relaxation of the film, while there is still some contribution from the top Ta cap and the oxide layer on top of it.

Diffusion in metallic glasses differs from that in crystals (Fig. 7). There are no distinct vacancies in metallic glasses, and diffusion is a result of local cooperative atomic motion (Fig. 7b) [21].

The diffusion rate strongly depends on the amount of excess volume stored in the glass [41], and for unrelaxed glasses, the diffusion coefficient decreases with time [42]. In multilayer thin
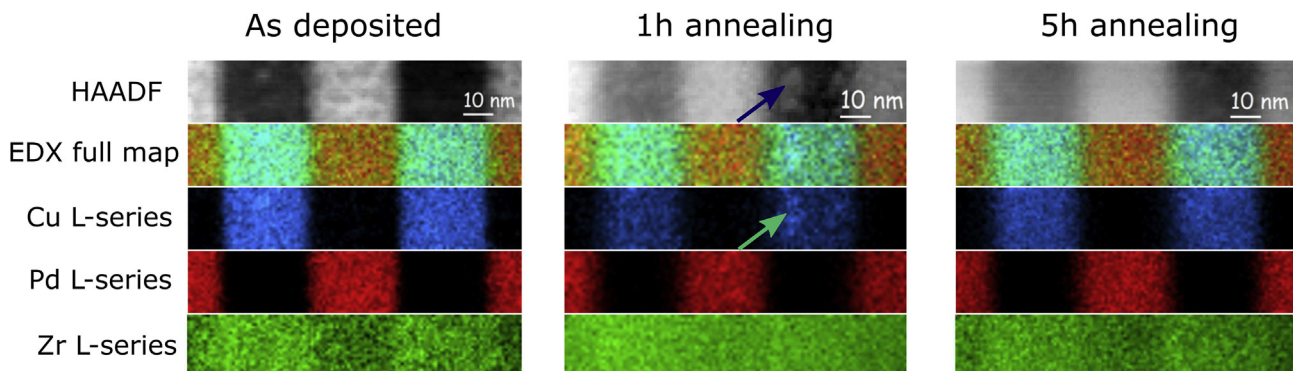

Fig. 4. EDX mappings and corresponding HAADF images of the film before and after annealing. Copper NCs are marked by arrows. EDX, energy-dispersive X-ray; HAADF, high-angle annular dark-field.
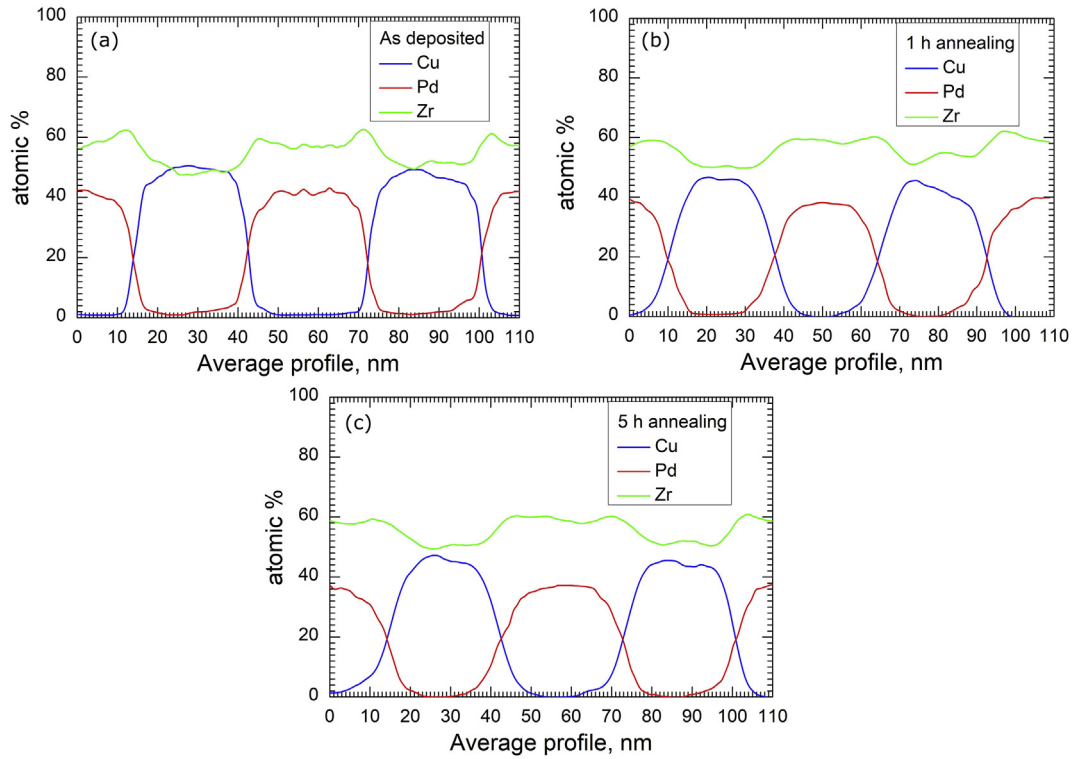
Fig. 5. Averaged chemical composition distribution curves: as-deposited film (a), after 1-h annealing (b), after 5-h annealing (c).
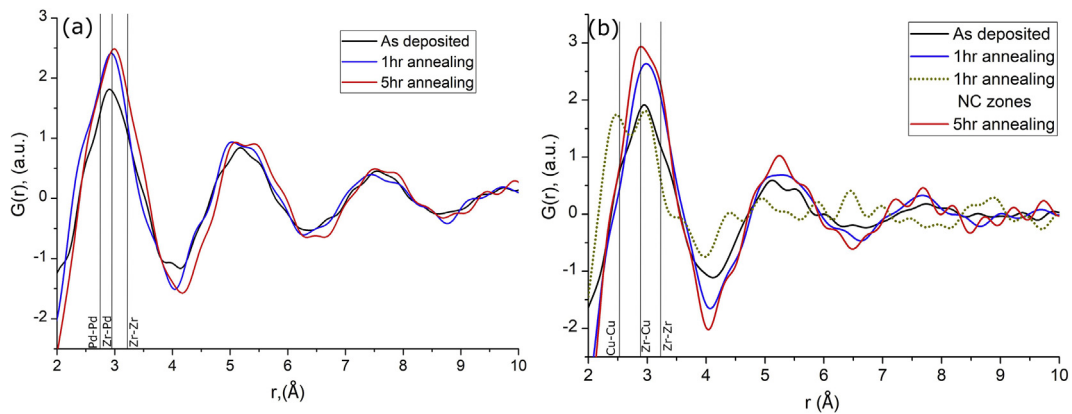

Fig. 6. Reduced radial atomic distribution functions (RRDF) for (a) the Zr-Pd and (b) the Zr-Cu layers. NC, nanocrystal.

Table 1
Results of nanoindentation tests of the multilayer films.

Sample treatment	E (GPa)	Apparent hardness (GPa)
As-deposited	111 ± 2	8.0 ± 0.2
After 1 h of annealing	112 ± 3	8.9 ± 0.4
After 5 h of annealing	118 ± 3	10.0 ± 0.6

films, the confinement also can play a significant role. It was found that, on one hand, covering of metallic glasses by a film containing heavy atoms can hinder the relaxation of metallic glass and preserve excess volume in the amorphous film [43] which might enhance initial diffusion. On the other hand, changes happening at the interface may change the thermodynamic potential driving the diffusion and increase the atomic stress level inside the film layers. Both of these parameters have a detrimental effect on diffusion

[19,44]. The analysis of the distribution profiles of copper and palladium in the present work (see Supplementary materials) shows that they have similar diffusion coefficients (Table 2) and the diffusion slows with increasing annealing time.

The diffusion coefficients even at such high annealing temperatures are significantly lower than those found for bulk diffusion of Co and Ni in Zr-based BMGs ($\sim 10^{-18}$ m^2/s) [21]. However, the values are comparable with that calculated for Ni in Zr-Ni thin films for the same film thickness [19]. However, the annealing temperature in our experiments was much higher, and therefore, diffusion is exceptionally slow in this case. In the present work, Zr and Pd are large and heavy atoms with low diffusivity, and in general, Cu atoms upon diffusion into Zr-Pd layer indeed should leave some pseudovacancies and small voids behind. However, owing to the physical constraints, diffusion of copper into Zr-Pd is limited. It may be partly connected to the effect of Ta which in analogy with W [43]
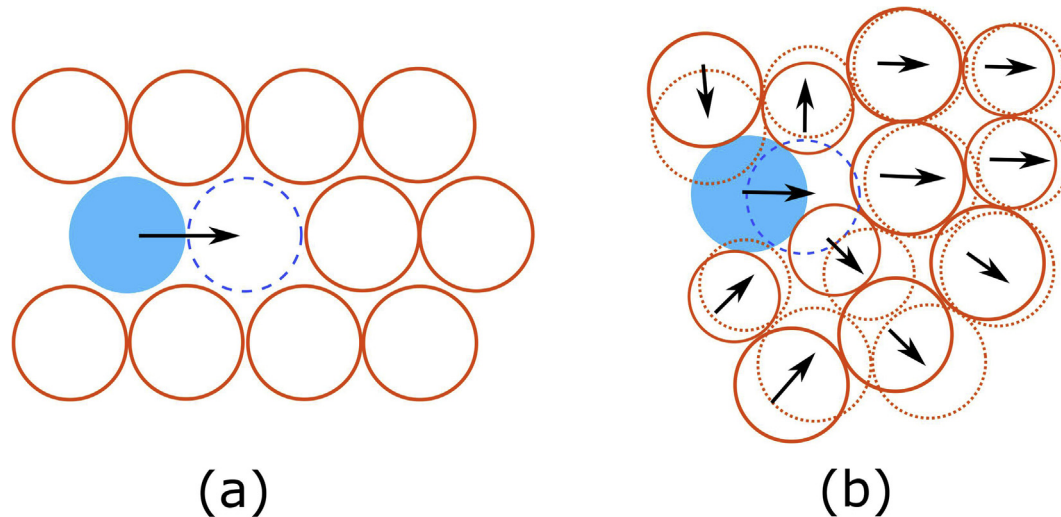
Fig. 7. Schematic illustration depicting diffusion of blue atom in an ordered crystal via vacancy mechanism (a) and in amorphous binary material by atomic collective motion (b). Dotted circles show the final position of the atoms and arrows show the movement direction.

Table 2
Diffusion coefficients calculated (Suppl. Fig. S5) from the concentration profiles from Fig. 5.

Element	D, m^2/s	
	0–1 h	1–5 h
Pd	1.2×10^{-21}	8.8×10^{-23}
Cu	1.4×10^{-21}	9.0×10^{-23}

covers the surface and does not allow the excess free volume to sink easily, only to redistribute inside the sample, although the ends are not covered.

Here, we should mention the other element that always can be found in sputtered films—argon. In the present work, it was the working gas in the sputtering process. Irradiated crystalline materials can trap helium inside the bulk, and upon annealing, the helium bubbles that form then act as nucleation sites for nanovoid growth by draining the vacancies from the surrounding area [45,46]. In the present work, the tantalum cap and the difference in the compositions of the glassy layers act to confine the system, not allowing effective relaxation, thus trapping the excess volume in the film layers. It is proposed that the trapped Ar atoms serve as nucleation sites for nanovoids which grow via attracting excess volume while relaxing the glass.

Molecular dynamics (MD) simulations show a similar behavior (Fig. 8). For these studies, Zr$_{50}$Cu$_{50}$ glass was modeled. A pore with a radius of 2 nm was placed inside the glass, and then the glass was annealed at near the glass-transition temperature T_g, under fixed container walls to simulate the constrained conditions.

One can notice that the pore radius grows upon annealing from 2 nm to 2.5 nm and copper tends to segregate on the surface of the pore. The annealing temperature is quite high, but the diffusion is still too slow and takes a lot of calculation time for the MD simulation. Therefore, we could not observe the crystallization of the copper on the surface of the pore. The amount of copper after 60 ns of simulation in the surface layer increased to 87 at.% (see Supplementary materials). We believe that further simulation for longer times would lead to the surface crystallization of the copper. A similar copper segregation was reported to take place in the surface layer of Zr-Cu-Al glass [47]. It is also commonly observed in nanoglasses [48]. Interestingly, the pore closes and the copper enrichment dissolves after the removal of the constraints. The

formation of these pores initially promotes internal self-diffusion and fast relaxation of the glass. However, such small voids are unstable, and on latter stages, they disappear. Formation of the copper crystals on the surface of the voids reduces the visibility of the voids in TEM due to their high order and high diffraction intensity.

In conclusion, interdiffusion between Zr-Pd and Zr-Cu layers in multilayered glassy film has been studied in the present work. The layers of both compositions retain their amorphous structure even at the annealing temperature of 400 °C which is close to their glass-transition temperatures. During annealing, interdiffusion of both copper and palladium between the layers was observed, whereas the mobility of zirconium atoms remains low. The calculated diffusion coefficients of Cu and Pd are very close to each other and decrease with increasing annealing time. No void formation distinguishable by HRTEM was found in the multilayered films. Annealing for 1 h results in the formation of agglomerates of pure copper crystalline nanoclusters which dissolve at longer annealing times. This finding is associated with the complex stress state evolution and relaxation of the multilayers. We could not observe void formation in the film layers. Segregation and crystallization of copper on the surface of the voids reduces their visibility due to the high diffraction intensity of the ordered copper. The formation of such voids and crystalline agglomerates can be beneficial for improving the plasticity of metallic glass/glass composites. We also demonstrate that aberration-corrected HRTEM images can be used to extract the RRDF curves of the particular chosen zones of metallic glasses with high resolution unachievable by any other methods. This allows extraction of information on the changes in the local atomic structure of amorphous materials.

3. Methods and materials

Films with a layered structure were deposited on fused silica substrates. The deposition was performed by radio frequency magnetron sputtering in high purity (99.9999%) under Ar atmosphere. The initial pressure in the chamber was 3×10^{-4} Pa. The sputtering Ar pressure was 4 Pa. Sputtering power was 100 W. Sputtering was performed from two pure Zr targets (99.9%) with sheet-shaped pieces (thickness of about 1 mm) of Cu and Pd on top of them and Ta (99.9%) target. Multilayers were obtained by rotating the substrate from one target to another and subsequent
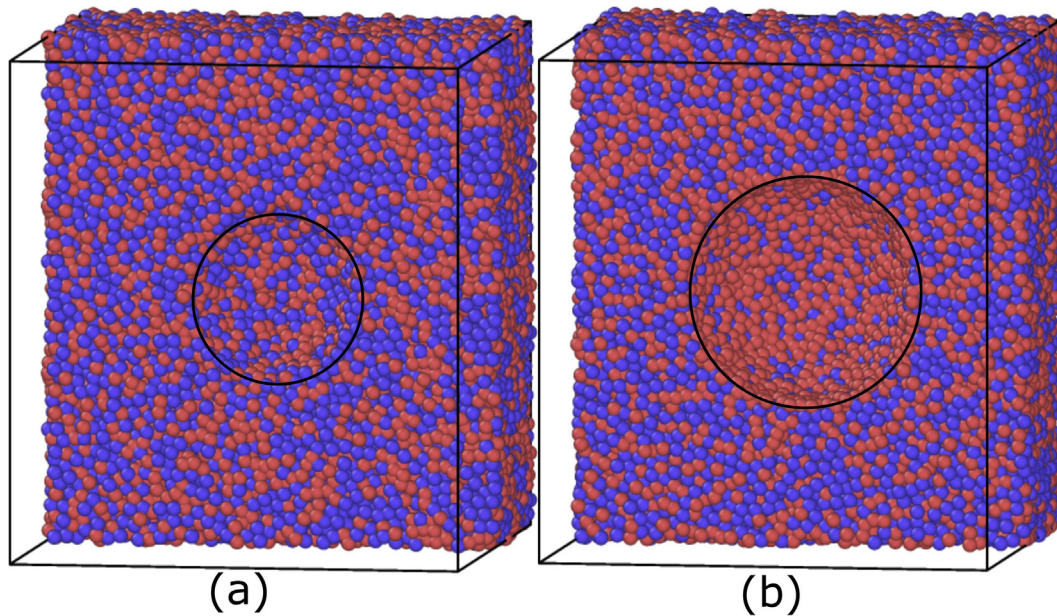
Fig. 8. MD simulation results of the behavior of a pore in constrained $Zr_{50}Cu_{50}$ metallic glass: (a) 0 ns, (b) after 60 ns near T_g. Here, red and blue spheres represent Cu and Zr atoms, respectively. The black lines are a guide for the eyes to evaluate the pore size. MD, molecular dynamics.

deposition. Substrate size was about $20 \times 20 \text{ mm}^2$. The films consisted of 5 layers of each composition with a thickness of the single layers of about 30 ± 1 nm. To protect the films from oxidation and Si diffusion, a tantalum cap (around 20 nm in thickness) was sputtered as the first and last layers without breaking the vacuum (Fig. 9). EDX spectroscopy analysis revealed that the compositions of the layers (at.%) are $Zr_{54}Cu_{46}$ and $Zr_{62}Pd_{38}$, respectively. The composition measurement has an error of ± 1 at.%. X-ray diffraction with Cu Kα characteristic radiation showed that the films were fully amorphous. The multilayer films were annealed at 400 °C inside the deposition chamber under vacuum for 1 and 5 h. As-deposited and annealed films were subsequently subjected to extensive TEM investigations.

The nanoindentation tests were conducted on a Hysitron Triboscope system (Bruker, Billerica, MA, USA). The transducer was mounted on the scanner head of a Digital Instruments D3100

Fig. 9. Schematic view of the multilayer and TEM sample which is shown in Fig. 1. Here not all layers are drawn. TEM, transmission electron microscopy.

device (Bruker). A diamond cube corner indenter was used for the measurements. Its area function was calibrated using a standard fused silica sample. A set of indentations, starting with a linear ramp up to the maximum load within 2 s, followed by holding the maximum load for 10 s, and finally unloading to zero load within 2 s, was performed. The maximum load for each sample was varied between 400 and 12000 μN. The fast loading and unloading sequences were chosen to minimize the influence of thermal instrumental drift, and the duration at the maximum load was chosen to minimize the influence of creep during unloading. The indentation depth for hardness calculations was chosen to be 50 nm. Hardness and elastic modulus were determined using the standard methods [49].

TEM studies were carried out with a Titan G2 60−300 (FEI, The Netherlands), equipped with a high-brightness field-emission gun and Cs image corrector. The estimated spatial resolution is about 0.08 nm at 300 kV. Images were acquired with a Gatan US1000 CCD camera. A dual-beam (ion beam and electron beam) system (FEI Helios 450) was used to fabricate the cross-sections of the samples. The EDX experiments were performed with an EDX RTEM (EDAX) detector using a probe size of around 0.5 nm. The electron-energy-loss spectroscopy (EELS) experiments were performed with a postcolumn high-resolution energy-filtering spectrometer (Gatan) to obtain the thickness of the area of interest from zero-loss spectrum imaging. The beam conditions of the microscope for EELS imaging and spectroscopy were defined to obtain a probe-size of 0.2 nm, with a convergence semiangle of 10 mrad and a collection semiangle of 12 mrad.

In the present study, the atomic RRDFs of the samples were directly calculated from the FFT patterns of the HRTEM images. Cs image correction allows extraction of information on the atomic structure evolution of amorphous materials from any area of interest, for instance nanoscale layers of different materials or small regions with agglomerating NCs. To obtain a clear FFT pattern, the thickness of the TEM sample must be less than 40 nm. Square areas with an edge size of 3.0 nm, randomly distributed on the HRTEM images, were chosen to build by FFT the diffraction patterns of the Cu-Zr and Pd-Zr layers after different annealing times. The averaging has been performed for 10 areas. The control of the sample
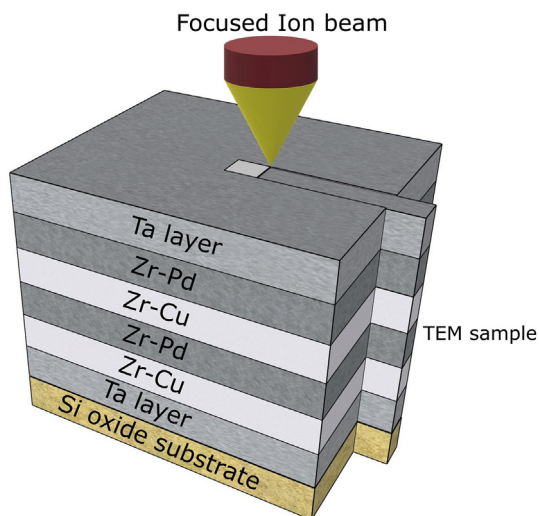
orientation relatively to the beam position was performed by following the protocol of the lamella preparation. The TEM specimen was extracted from the sample perpendicular to the surface of the substrate by focused ion beam milling, placed, and finally milled on the TEM grid keeping the orientation of the specimen as parallel as possible to the plane of the grid. A final check was performed by tilting the sample inside the TEM column using the sharp interface between polycrystalline Ta layer and Si oxide substrate as a reference.

The effect of pressure on the process of crystal dissolution in the $Zr_{64}Cu_{36}$ metallic glass was analyzed by MD simulations using the code LAMMPS [50]. No suitable interatomic potentials are available for the Zr-Cu-Pd system; hence, we selected the $Zr_{50}Cu_{50}$ composition because for this composition a reliable Finnis–Sinclair type potential developed by Mendelev et al. exists [51]. The simulated specimen was generated as follows: first, a metallic-glass cubic cell containing 8000 atoms was produced by quenching from the melt to 850 K with a cooling rate of 10^{10} K/s. A cubic sample with dimensions $11 \times 11 \times 11$ nm^3 was then created by replicating the initial glass cubic cell, giving a total number of atoms of about 64000. A spherical pore with a radius of 2 nm was placed inside the glassy cubic cell. Periodic boundary conditions were applied along all three directions. The size of the cell was kept constant during the simulation. The atomic structure during relaxation was investigated using Common Neighbor Analysis calculated by the OVITO analysis and visualization software [52].

Data availability

The raw data required to reproduce these findings are available to download from: https://doi.org/10.17632/fsfsmtxgbc.1.

Conflict of interests

The authors declare that they have no known competing financial interests or personal relationships that could have appeared to influence the work reported in this paper.

Funding

Acknowledgments

Appendix A. Supplementary data

Supplementary data to this article can be found online at https://doi.org/10.1016/j.mtadv.2019.01.003.

References

[1] A. Inoue, A. Takeuchi, Recent development and application products of bulk glassy alloys, Acta Mater. 59 (2011) 2243–2267.

[2] M.M. Trexler, N.N. Thadhani, Mechanical properties of bulk metallic glasses, Prog. Mater. Sci. 55 (2010) 759–839.

[3] C.A. Schuh, T.C. Hufnagel, U. Ramamurty, Mechanical behavior of amorphous alloys, Acta Mater. 55 (2007) 4067–4109.

[4] T.C. Hufnagel, C.A. Schuh, M.L. Falk, Deformation of metallic glasses: recent developments in theory, simulations, and experiments, Acta Mater. 109 (2016) 375–393.

[5] K. Georgarakis, M. Aljerf, Y. Li, A. LeMoulec, F. Charlot, A.R. Yavari, K. Chornokhvostenko, E. Tabachnikova, G.A. Evangelakis, D.B. Miracle, A.L. Greer, T. Zhang, Shear band melting and serrated flow in metallic glasses, Appl. Phys. Lett. 93 (2008) 031907.

[6] A.L. Greer, Y.Q. Cheng, E. Ma, Shear bands in metallic glasses, Mater. Sci. Eng. R 74 (2013) 71–132.

[7] J. Eckert, J. Das, S. Pauly, C. Duhamel, Mechanical properties of bulk metallic glasses and composites, J. Mater. Res. 22 (2) (2007) 285–301.

[8] J. Qiao, H. Jia, P.K. Liaw, Metallic glass matrix composites, Mater. Sci. Eng. R 100 (2016) 1–69.

[9] J. He, I. Kaban, N. Mattern, K.K. Song, B.A. Sun, J. Zhao, D.H. Kim, J. Eckert, A.L. Greer, Local microstructure evolution at shear bands in metallic glasses with nanoscale phase separation, Sci. Rep. 6 (2016) 25832.

[10] S. Cardinal, J.M. Pelletier, G.Q. Xie, F. Mercier, Manufacturing of Cu-based metallic glasses matrix composites by spark plasma sintering, Mater. Sci. Eng. A 711 (2018) 405–414.

[11] M. de Oliveira, W.J. Botta F, A.R. Yavari, Connecting, assemblage and electro-mechanical shaping of bulk metallic glasses, Mater. Trans. 41 (2000) 1501–1504.

[12] D.V. Louzguine-Luzgin, G.Q. Xie, T. Tsumura, H. Fukuda, K. Nakata, H.M. Kimura, A. Inoue, Structural investigation of Ni–Nb–Ti–Zr–Co–Cu glassy samples prepared by different welding techniques, Mater. Sci. Eng. B 148 (2008) 88–91.

[13] T. Tsumura, K. Nakata, Laser welding of Ni-based metallic glass foil, Weld. Int. 25 (2011) 491–496.

[14] Y. Yokoyama, N. Abe, K. Fukaura, A. Inoue, Electron beam welding of $Zr_{50}Cu_{30}Ni_{10}Al_{10}$ bulk glassy alloys, Mater. Trans. 43 (2002) 2509–2515.

[15] D.V. Louzguine-Luzgin, Y. Yokoyama, G. Xie, N. Abe, A. Inoue, Transmission electron microscopy investigation of the structure of a welded $Zr_{50}Cu_{30}$-$Ni_{10}Al_{10}$ glassy alloy sample, Philos. Mag. Lett. 87 (2007) 549–554.

[16] T. Shoji, Y. Ohno, Y. Kawamura, Joining of $Zr_{41}Be_{23}Ti_{14}Cu_{12}Ni_{10}$ bulk metallic glasses by a friction welding method, Mater. Trans. 44 (2003) 1809–1816.

[17] S. Herd, K.N. Tu, K.Y. Ahn, Formation of an amorphous RhSi alloy by interfacial reaction between amorphous Si and crystalline Rh thin films, Appl. Phys. Lett. 42 (1983) 597–599.

[18] R.B. Schwarz, W.L. Johnson, Formation of an amorphous alloy by solid-state reaction of the pure polycrystalline metals, Phys. Rev. Lett. 51 (1983) 415–418.

[19] A.L. Greer, N. Karpe, J. Bøttiger, Diffusional aspects of the solid state amorphization reaction, J. Alloys Comp. 194 (1993) 199–211.

[20] N. Karpe, J. Bøttiger, A.L. Greer, J. Janting, K. Kyllesbech Larsen, On the chemical diffusion in layered thin films containing amorphous Co-Zr, Ni-Zr, and Fe-Zr, J. Mater. Res. 7 (1992) 926–933.

[21] F. Faupel, W. Frank, M.-P. Macht, H. Mehrer, V. Naundorf, K. Rätzke, H.R. Schober, S.K. Sharma, H. Teichler, Diffusion in metallic glasses and supercooled melts, Rev. Mod. Phys. 75 (2003) 237–280.

[22] J.G. Wang, J.C. Fan, Y.F. Zhang, G. Wang, W.H. Wang, K.C. Chan, Diffusion bonding of a Zr-based metallic glass in its supercooled liquid region, Intermetallics 46 (2014) 236–242.

[23] Ch Wen, T. Shi, B. Chen, Zh Zhu, Y. Peng, G. Liao, Diffusion bonding of $Zr_{55}Cu_{30}Ni_5Al_{10}$ bulk metallic glass to Cu with Al as transition layer, Mater. Des. 83 (2015) 320–326.

[24] L.L. Sun, J. Wang, H.C. Kou, B. Tang, J.S. Li, P.X. Zhang, Interface characteristics of a Zr-based BMG/copper laminated composite, Surf. Interface Anal. 46 (2014) 61–64.

[25] Y. Zhang, C.Z. Wang, M.I. Mendelev, F. Zhang, M.J. Kramer, K.M. Ho, Diffusion in a Cu-Zr metallic glass studied by microsecond-scale molecular dynamics simulations, Phys. Rev. B 91 (2015) 180201(R).

[26] Y. Zhu, G. Liao, T. Shi, Z. Tang, M. Li, Interdiffusion cross crystal-amorphous interface: an atomistic simulation, Acta Mater. 112 (2016) 378–389.

[27] M. Sun, A. Rauf, Y. Zhang, G. Sha, G. Peng, Zh Yu, Ch Guo, Y. Fang, S. Lan, T. Feng, H. Hahn, H. Gleiter, Enhanced inter-diffusion of immiscible elements Fe/Cu at the interface of FeZr/CuZr amorphous multilayers, Mater. Res. Lett. 6 (2017) 55–60.

[28] A.D. Smigelskas, E.O. Kirkendall, Zinc diffusion in alpha brass, Trans. AIME 171 (1947) 130–142.

[29] F. Seitz, On the porosity observed in the Kirkendall effect, Acta Metall. 1 (1953) 355–369.

[30] T. Wada, A. Inoue, A.L. Greer, Enhancement of room-temperature plasticity in a bulk metallic glass by finely dispersed porosity, Appl. Phys. Lett. 86 (2005) 251907.

[31] K.N. Tu, T.C. Chou, Submicron void formation in amorphous NiZr Alloys, Phys. Rev. Lett. 61 (1988) 1863–1866.

[32] L. Yang, G.-Q. Guo, J.-Z. Jiang, L.-Y. Chen, S.-H. Wei, "Soft" atoms in $Zr_{70}Pd_{30}$ metal–metal amorphous alloy, Scripta Mater. 63 (2010) 883–886.

[33] G.-Q. Guo, S.-Y. Wu, S. Luo, L. Yang, Detecting structural features in metallic glass via synchrotron radiation experiments combined with simulations, Metals 5 (2015) 2093–2108.

[34] B.S. Murty, D.H. Ping, M. Ohnuma, K. Hono, Nanoquasicrystalline phase formation in binary Zr−Pd and Zr−Pt alloys, Acta Mater. 49 (2001) 3453−3462.

[35] M.M. Khandpekar, A. Shrivastava, D.S. Gowtam, M. Mohape, V.P. Deshmukh, Prediction of glass forming ability in Cu_xZr_{1-x} alloys using molecular dynamics, Nanosystems 6 (5) (2015) 650−660.

[36] P. Zeman, M. Zítek, S. Zuzjakov, R. Cerstvý, Amorphous Zr-Cu thin-film alloys with metallic glass behavior, J. Alloys Comp. 696 (2017) 1298−1306.

[37] Yoshihiro Takahara, Nobutaka Narita, Local electronic structures and chemical bonds in Zr-based metallic glasses, Mater. Trans. 45 (4) (2004) 1172−1176.

[38] D.R.G. Mitchell, T.C. Petersen, RDFTools, A software tool for quantifying short-range ordering in amorphous materials, Microsc. Res. Techn. 75 (2012) 153−163.

[39] A. Takeuchi, A. Inoue, Classification of bulk metallic glasses by atomic size difference, heat of mixing and period of constituent elements and its application to characterization of the main alloying element, Mater. Trans. 46 (2005) 2817−2829.

[40] N. Mattern, P. Jóvári, I. Kaban, S. Gruner, A. Elsner, V. Kokotin, H. Franz, B. Beuneu, J. Eckert, Short-range order of Cu−Zr metallic glasses, J. Alloys Comp. 485 (2009) 163−169.

[41] J. Bokeloh, S.V. Divinski, G. Reglitz, G. Wilde, Tracer measurements of atomic diffusion inside shear bands of a bulk metallic glass, Phys. Rev. Lett. 107 (2011) 235503.

[42] J. Bøttiger, N.G. Chechenin, N. Karpe, J.P. Krog, Diffusion in thin-film amorphous metallic alloys, Nucl. Instr. Meth. Phys. Res. B 85 (1994) 206−215.

[43] Z.Q. Chen, L. Huang, F. Wang, P. Huang, T.J. Lub, K.W. Xua, Suppression of annealing-induced embrittlement in bulk metallic glass by surface crystalline coating, Mater. Des. 109 (2016) 179−185.

[44] N. Karpe, J.P. Krog, J. Bøttiger, N.G. Chechenin, R.E. Somekh, A.L. Greer, The thermodynamic factor in interdiffusion: a strong effect in amorphous Ni-Zr, Acta Metall. 43 (1995) 551−558.

[45] K.F. Kelton, A.L. Greer, Nucleation in Condensed Matter, Pergamon, 2010.

[46] H. Zhang, F. Ren, Y. Wang, M. Hong, X. Xiao, W. Qin, Ch Jiang, In situ TEM observation of helium bubble evolution in V/Ag multilayer during annealing, J. Nucl. Mater. 467 (2015) 537−543.

[47] D.V. Louzguine-Luzgin, C.L. Chen, L.Y. Lin, Z.C. Wang, S.V. Ketov, M.J. Miyama, A.S. Trifonov, A.V. Lubenchenko, Y. Ikuhara, Bulk metallic glassy surface native oxide: its atomic structure, growth rate and electrical properties, Acta Mater. 97 (2015) 282−290.

[48] O. Adjaoud, K. Albe, Interfaces and interphases in nanoglasses: surface segregation effects and their implications on structural properties, Acta Mater. 113 (2016) 284−292.

[49] W.C. Oliver, G.M. Pharr, An improved technique for determining hardness and elastic modulus using load and displacement sensing indentation experiments, J. Mater. Res. 7 (1992) 1564−1583.

[50] S.J. Plimpton, Fast parallel algorithms for short-range molecular dynamics, J. Comput. Phys. 117 (1995) 1−19.

[51] M.I. Mendelev, D.J. Sordelet, M.J. Kramer, Using atomistic computer simulations to analyze x-ray diffraction data from metallic glasses, J. Appl. Phys. 102 (2007) 043501.

[52] A. Stukowski, Visualization and analysis of atomistic simulation data with Ovito-the open visualization tool, Modell. Simul. Mater. Sci. Eng. 18 (1) (2010) 015012.